Organic ligands and CeO_2-induced generic valence modulation strategies to design Fe active sites for promoted oxygen involved reactions in rechargeable zinc–air batteries†

Jiao Peng,‡[a] Zining Wang,‡[b] Jianwei Ren,*[c] Yudong He,[a] Jiahao Li,[a] Shichang Xin,[a] Xuyun Wang,[a] Hui Wang*[a] and Rongfang Wang*[a]

* Corresponding authors

[a] State Key Laboratory Base for Eco-Chemical Engineering, College of Chemical Engineering, Qingdao University of Science and Technology, Qingdao, China **E-mail:** wangh@qust.edu.cn, rfwang@qust.edu.cn

[b] School of Chemical Science and Engineering, Tongji University, Shanghai 200092, China

[c] Department of Chemical Engineering, University of Pretoria, Cnr Lynnwood Road and Roper Street, Hatfield 0028, South Africa. E-mail: jianwei.ren@up.ac.za

‡ These authors contributed equally to this work.

Abstract

The limited catalytic selectivity and stability of most metal oxides during reactions are primarily due to their irreversible valence transitions. To address this challenge, this study focuses on the development of CeO_2-induced valence-tunable Fe_xO nanoparticles, which were supported on a nitrogen-doped carbon substrate to enhance the catalytic performance of the oxygen reduction reaction (ORR) and the oxygen evolution reaction (OER). *In situ* Raman spectroscopy confirmed that the key intermediates involved in the ORR on the CeO_2–Fe_xO/NC catalyst surface are $*O_2^-$ and *OOH, which remain stable even at low potentials. Ultraviolet photoelectron spectroscopy (UPS) revealed that the CeO_2–Fe_xO/NC catalyst exhibits a lower work function, which facilitates electron escape and promotes the activation of oxygen molecules. X-ray photoelectron spectroscopy (XPS) further showed that Fe in CeO_2–Fe_xO/NC has a reduced binding energy, with Fe_xO acting as a broad valence electron reservoir (0–3 e^-), which enhances proton-coupled electron transfer and accelerates reaction kinetics during the catalytic process. As a result, the CeO_2–Fe_xO/NC sample demonstrates outstanding bifunctional oxygen electrocatalytic performance, with a potential gap of just 0.62 V, surpassing that of the Pt/C + RuO_2 catalyst (0.65 V). Moreover, zinc–air batteries utilizing the CeO_2–Fe_xO/NC catalyst exhibit a high specific capacity of 743.0 mA h g^{-1}.

Introduction

The depletion of fossil fuels and the escalating environmental challenges have spurred the advancement of sustainable energy conversion technologies, including metal–air batteries and fuel cells.[1–3] The slow reaction rates of the oxygen reduction reaction (ORR) and oxygen evolution reaction (OER), along with the substantial overpotentials they demand, pose considerable challenges in the field of electrocatalysis.[3–6] Currently, catalysts derived from noble metals are regarded as the most effective for facilitating both the ORR and OER.

However, their high cost, limited availability, and poor stability at optimal voltages significantly restrict their widespread use.[7–9] Consequently, extensive research efforts have been focused on identifying high-performance non-noble metal bifunctional electrocatalysts. Among these, iron-based catalysts have emerged as some of the most efficient non-noble metal options for the ORR.[10–13] Compared to monometallic catalysts, bimetallic modifications frequently demonstrate enhanced catalytic performance. Recent studies have largely concentrated on modifying crystal structures, morphologies, and supports to improve catalytic efficiency.[14–16] Given the d-orbital electron configurations of transition metals (TMs), their metal centers often exhibit multiple valence states, which can be leveraged to optimize their electronic properties and catalytic activity.[17–19] As a result, controlling the valence states of TMs has become a recognized strategy to improve catalyst performance in electrocatalytic processes. For instance, copper (Cu) has been widely studied due to its ability to exist in multiple valence states and its role in photoinduced interfacial charge transfer processes.[20,21] Moon *et al.*[22] demonstrated that metallic Cu, produced by reducing CuO, acts as an effective cocatalyst to enhance hydrogen (H_2) production. In a similar study, Guan *et al.*[23] employed unsaturated tungsten oxides (W^{5+}, W^{6+}) and vacancy engineering to modify the electronic structure of catalyst surfaces, thus accelerating catalytic reactions. At the same time, the introduction of metallic tungsten (W^0) boosted the catalyst's conductivity. $MnCo_xO_4$/NCNT has also been reported as a highly effective bifunctional oxygen electrocatalyst, owing to the multivalent Co and Mn ions in $MnCo_xO_4$, which help modulate the catalyst's electronic properties and enhance electrocatalytic activity.[20] Liu *et al.*[24] explored the relationship between multivalent metals and their effects on hydrogen evolution reaction (HER) and urea oxidation reaction (UOR) performance, finding that Mo^{5+} and Ni^{3+} act as active sites for the HER and UOR, respectively, thus promoting faster catalytic kinetics. Zhao *et al.*[18] highlighted the influence of vanadium's (V) multivalent states on the electrochemical nitrogen reduction reaction (ENRR) activity of VS_x, showing that V^{4+} provides more delocalized electrons for charge exchange than V^{2+}, leading to a reduction in the energy barriers for nitrogen (N_2) adsorption and activation. Similarly, Ye *et al.*[19] developed a multivalent two-dimensional MoS_2/Mo_2C electrocatalyst with a specific Mo^{3+} valence state. The well-defined interfacial charge transfer from metallic Mo_2C to semiconducting MoS_2 significantly improved nitrogen reduction reaction (NRR) performance.

Building upon the concepts outlined above, this study developed a bimetallic catalyst, CeO_2–Fe_xO/NC, that utilizes strong metal–ligand interactions to achieve efficient catalysis for both the ORR and OER. *In situ* Raman spectroscopy revealed the dynamic evolution of $*O_2^-$ and *OOH on CeO_2–Fe_xO/NC at various potentials. The multivalent states of Fe were precisely controlled through the synergistic interaction between CeO_2 and phenanthroline (PM), where PM, as a bidentate nitrogen ligand, formed stable complexes with Fe^{2+} and Ce^{3+}, effectively anchoring the metal active sites. Furthermore, a clear charge transfer from CeO_2 to Fe_xO facilitated the generation of low-valence Fe, resulting in a wide valence range spanning Fe^0 to Fe^{3+}. This multivalent Fe significantly enhanced the catalytic kinetics by modulating the electronic properties. As a result, the CeO_2–Fe_xO/NC catalyst demonstrated exceptional bifunctional oxygen electrocatalytic performance, with a half-wave potential of 0.89 V and an overpotential of 276 mV at a current density of 10 mA cm^{-2}. Additionally, zinc–air batteries (ZABs) assembled with CeO_2–Fe_xO/NC exhibited excellent long-term stability exceeding 200 h.

Experimental section

Synthesis of the nitrogen-doped porous carbon (NC) sample

To synthesize nitrogen-doped porous carbon (NC), 1 g of peptone was mixed with 10 g of calcium chloride and ball-milled for 1.5 h to ensure thorough blending. The resulting mixture was then placed in a tube furnace and heated up to 900 °C in a nitrogen (N_2) atmosphere at a heating rate of 5 °C min^{-1}. The temperature was maintained for 1 h, and subsequently the furnace was allowed to cool down naturally. The product was washed with water to remove excess calcium chloride and subjected to three acid washes with 1 M hydrochloric acid (HCl). The sample was then rinsed with water until a neutral pH was achieved, resulting in the formation of the NC material.

Synthesis of the CeO_2–Fe_xO/NC sample

A mixture containing 80 mg of NC, 0.2 mL (0.02 mmol) of $Fe(PM)_3^{2+}$, 0.2 mL (0.002 mmol) of $Ce(PM)_4^{4+}$, and 5 mL of water was homogenized and then dried in an oven at 90 °C for 3 h. The dried mixture was subsequently pyrolyzed at 700 °C for 1 h, following the same heating rate. After pyrolysis, the sample was collected to yield the final CeO_2–Fe_xO/NC catalyst. To prepare the precursor solutions, the 0.1 M $Fe(PM)_3^{2+}$ solution was prepared by dissolving 0.198 g of $FeCl_2 \cdot 4H_2O$ and 0.595 g of PM in 10 mL of water. Similarly, the 0.01 M $Ce(PM)_4^{4+}$ solution was obtained by dissolving 0.0548 g of $Ce(NH_4)_2(NO_3)_6$ and 0.0793 g of PM in 10 mL of water.

Synthesis of Ce–Fe_xO/NC and other samples

To prepare a control sample without the addition of PM ($C_{12}H_8N_2 \cdot H_2O$), Ce–Fe_xO/NC was synthesized by mixing 80 mg of NC with 0.2 mL (0.02 mmol) of $FeCl_2 \cdot 4H_2O$, 0.2 mL (0.002 mmol) of $Ce(NH_4)_2(NO_3)_6$, and 5 mL of water. The mixture was processed under the same conditions described previously to obtain the Ce–Fe_xO/NC sample. For comparison with single-metal catalysts, a sample designated as Fe_xO/NC was prepared under identical conditions but without the addition of $Ce(NH_4)_2(NO_3)_6$. Details regarding the preparation of other samples are provided in Table S1.† Information about the characterization and electrochemical testing of the synthesized samples is detailed in the ESI.†

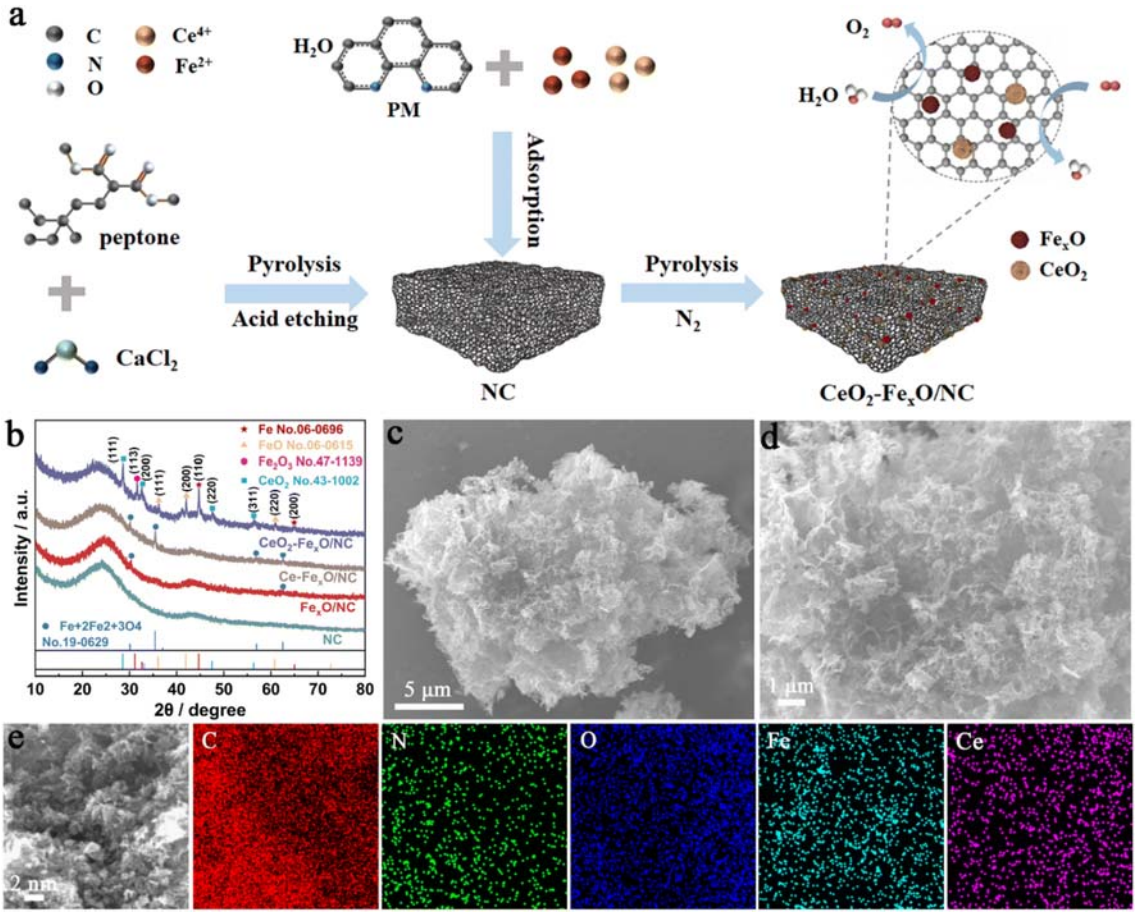

Fig. 1 CeO_2–Fe_xO/NC sample: (a) schematic illustration of the synthesis process. (b) X-ray diffraction (XRD) patterns. (c and d) Scanning electron microscopy (SEM) images and (e) elemental mapping images showing the distribution of key elements (C, N, O, Fe and Ce).

Results and discussion

The preparation process for the CeO_2–Fe_xO/NC catalyst is depicted in Fig. 1a. Initially, a porous nitrogen-doped carbon substrate is synthesized through a combination of ball milling, high-temperature pyrolysis, and acid washing. PM is then used to coordinate with Fe^{2+} and Ce^{3+} ions, forming metal complexes, which are subsequently mixed with the carbon substrate. The final high-temperature pyrolysis ensures the successful incorporation of metal nanoparticles into the nitrogen-doped carbon framework, resulting in the CeO_2–Fe_xO/NC catalyst. The crystal structure of the catalyst was characterized using XRD analysis. As shown in Fig. 1b, the CeO_2–Fe_xO/NC sample displays diffraction peaks at 28.5°, 33.1°, 47.5°, and 56.3°, corresponding to the (111), (200), (220), and (311) planes of CeO_2 (PDF#43-1002). The Fe species in the catalyst exist in multiple oxidation states, including Fe (PDF#06-0696), FeO (PDF#06-0615), and Fe_2O_3 (PDF#47-1139). This behavior can be attributed to PM acting as both a redox ligand and an electron reservoir, which regulates the oxidation states of Fe.[25] CeO_2 has the characteristic of reversible change between the valence states of Ce^{3+} and Ce^{4+}. Notably, the characteristic peaks of Ce–Fe_xO/NC and Fe_xO/NC samples correspond to the Fe + $2Fe_2$ + $3O_4$ phase (PDF#19-0629), which contrasts with the oxidation states of Fe in CeO_2–Fe_xO/NC. This suggests that the synergy between CeO_2 and PM facilitates the oxidation state transformation of Fe, shifting from Fe^0 to Fe^{3+}. All samples exhibit a broad diffraction peak at

25.1°, which is attributed to the (002) plane of amorphous carbon (PDF#41-1487). Bragg's equation was employed to calculate the interlayer spacing of the carbon.[26] Gaussian fitting results (Fig. S3 and Table S2†) indicate that, compared to other samples, the diffraction peak of the (002) plane in the CeO_2–Fe_xO/NC sample shifts to a higher angle (25.09°), closer to the (002) plane of graphene (diffraction peak angle = 26.4°, interlayer spacing = 3.4 Å). This shift suggests successful nitrogen doping into the carbon structure from PM, which leads to a modification in the interlayer distance of the carbon layers. The interlayer spacing of carbon in CeO_2–Fe_xO/NC is close to the ideal graphite layer spacing, optimizing the electronic conduction pathway of the material, which contributes to enhancing its electrical conductivity.

The morphology of the CeO_2–Fe_xO/NC catalyst was examined using field emission SEM and transmission electron microscopy (TEM). As shown in Fig. 1c and d, the CeO_2–Fe_xO/NC sample exhibits a well-defined porous and loose structure. Elemental mapping in Fig. 1e confirms that Fe and Ce are uniformly distributed across the nitrogen-doped carbon matrix. TEM images (Fig. 2a and b) reveal numerous metal nanoparticles dispersed randomly in the carbon matrix, with the nanoparticles clearly marked by red circles. In the TEM image of the Ce–Fe_xO/NC sample (Fig. S1†), no distinct metal particles were observed, suggesting that PM plays a role in anchoring the metal nanoparticles securely into the carbon matrix.[25,27] The TEM image of the NC sample in Fig. S2† displays a layered, porous structure of the carbon material. High-resolution transmission electron microscopy (HR-TEM) images of the CeO_2–Fe_xO/NC sample (Fig. 2d and e) show clear lattice fringes, indicating the high crystallinity of the nanoparticles. The interplanar spacings of 0.292 nm and 0.162 nm correspond to the (102) plane of Fe_2O_3 and the (311) plane of CeO_2, respectively (Fig. 2e). The HR-TEM images also reveal a prominent interface between the Fe_xO and CeO_2 components, which aligns with the selected area electron diffraction (SAED) patterns presented in Fig. 2h. Energy-dispersive X-ray spectroscopy (EDS) analysis (Fig. 2i) further confirms the elemental composition of CeO_2–Fe_xO/NC, which includes Fe, Ce, O, N, and C. This verifies the successful integration of Fe_xO and CeO_2 into the carbon matrix, thereby creating interfaces that modulate the electronic structure of the metal centers. The wettability of the electrode surface was assessed using contact angle measurements. The CeO_2–Fe_xO/NC catalyst was drop-cast onto a nickel foam substrate to fabricate the electrode material, which was then tested for mass transfer effects during the ORR and OER. After the OER (Fig. 2c), the water contact angle was measured to be 77.9°, indicating good interaction between the catalyst and the electrolyte.[5] Additionally, the bubble contact angle decreased by 35.5° from 135.0° (after the OER) to a lower value after the ORR (Fig. 2f). This suggests that, during the ORR process, O_2 is more easily transported to the electrode surface, facilitating the mass transfer of oxygen reactants in the gas diffusion layer.[28] Therefore, CeO_2–Fe_xO/NC provides an efficient mass transfer pathway during the reaction, enhancing the three-phase interface (gas absorption and release, exposure of active sites, and electrolyte transport).[29]

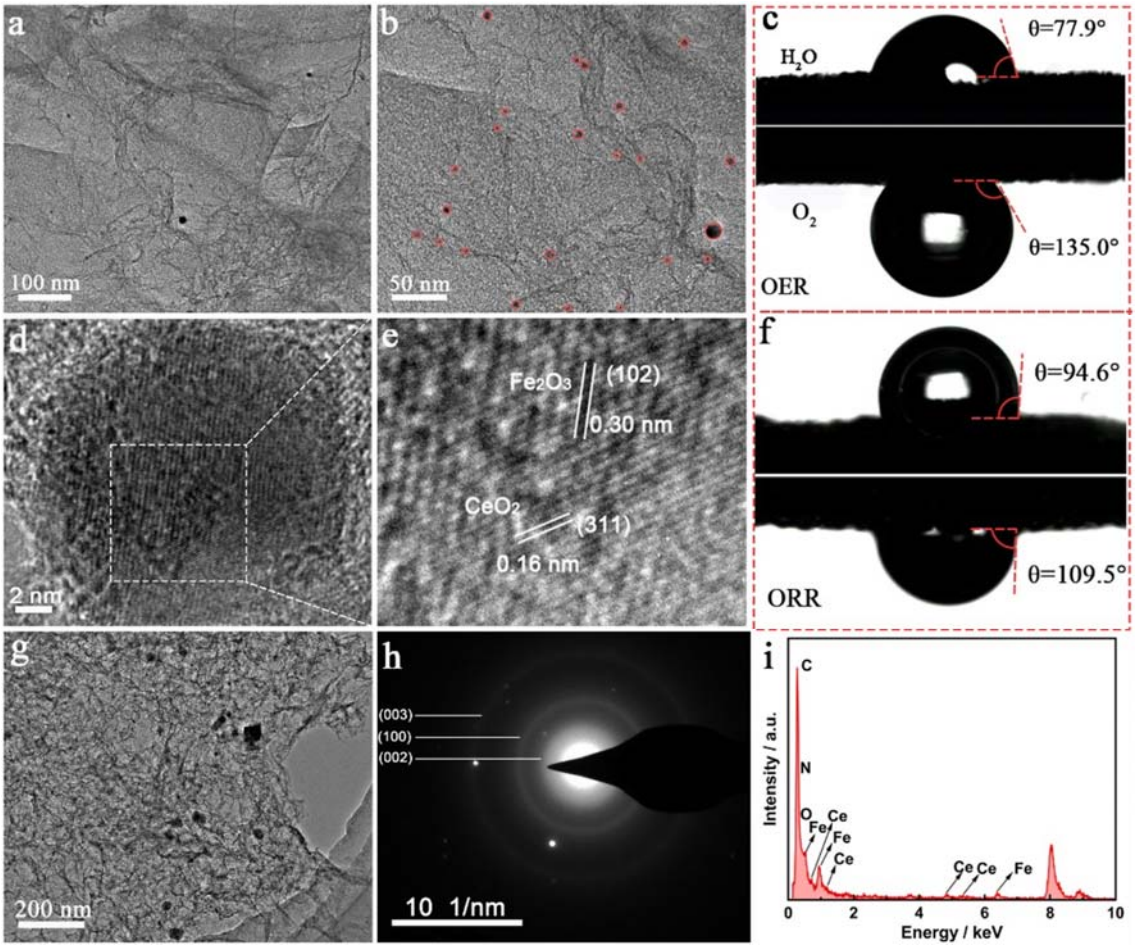

Fig. 2 (a, b and g) Transmission electron microscopy (TEM) images of the CeO_2–Fe_xO/NC sample. (c) Contact angle measurement after the OER at E_j = 50 mA cm^{-2} (1.59 V) for 3 h. (d and e) High-resolution transmission electron microscopy (HRTEM) images of the CeO_2–Fe_xO/NC sample. (f) Contact angle measurement after the ORR at $E_{1/2}$ = 0.89 V for 3 h. (h) SAED (selected area electron diffraction) spectra. (i) Energy-dispersive X-ray spectroscopy (EDS) spectrum of the CeO_2–Fe_xO/NC sample.

Raman spectroscopy, a non-destructive technique, was employed to characterize the structural properties of the carbon materials. As shown in Fig. S4,† the D band at 1362.05 cm^{-1} and the G band at 1592.23 cm^{-1} correspond to the disorder in sp^3 carbon and the in-plane vibrations of sp^2 carbon, respectively. The intensity ratio of I_D/I_G from the D and G bands is usually used to determine the level of defects in the carbon material.[30,31] A higher I_D/I_G ratio indicates a greater degree of defects. The I_D/I_G ratio of the CeO_2–Fe_xO/NC sample (1.08) is larger than that of the Fe_xO/NC (0.97) sample. The increase in defect density is attributed to the introduction of PM and the doping of CeO_2, effectively modifying the carbon defect structure of the CeO_2–Fe_xO/NC catalyst, which reflects a richer defect profile in the material. The N_2 adsorption–desorption isotherm of CeO_2–Fe_xO/NC (Fig. S5a†) exhibits characteristics of a type IV isotherm, which displays a sharp increase in nitrogen adsorption at low relative pressures (P/P_0) as well as a pronounced hysteresis loop between P/P_0 = 0.5–1.0. This indicates the presence of abundant micropores and mesopores in the CeO_2–Fe_xO/NC sample. The pore size distribution curve (Fig. S5b†) further confirms the coexistence of both micropores and mesopores in the material. When compared to other metal-based catalysts (Fig. S5c and d†), the CeO_2–Fe_xO/NC sample demonstrates a significantly higher specific surface area (1078.80 m^2 g^{-1}) and pore

volume (1.18 $cm^3\ g^{-1}$). This improvement is likely due to the extensive polymerization between PM and the metals, which helps preserve the integrity of the carbon pore channels and prevents their collapse during the pyrolysis process due to metal corrosion.[32] The high surface area of CeO_2–Fe_xO/NC enhances the exposure of active catalytic centers, while its mesoporous structure provides an efficient transport pathway for reactants and intermediates, thus facilitating the catalytic reaction.[33–35]

The electronic structure of CeO_2–Fe_xO/NC and Fe_xO/NC samples was investigated using Ultraviolet Photoelectron Spectroscopy (UPS) to evaluate the work function (Φ) and electron transfer properties of the catalysts. As shown in Fig. 3a and b, the work function of the CeO_2–Fe_xO/NC sample was calculated based on the secondary electron cutoff value (E_{cutoff}) and the Fermi level (E_F). In contrast, the work function of the CeO_2–Fe_xO/NC sample decreased by 0.45 eV compared to that of the Fe_xO/NC sample, suggesting that the incorporation of nitrogen and CeO_2 into the structure promotes electron transfer within the material. This reduction in work function facilitates the easier escape of electrons from the catalyst surface, thereby enhancing the catalytic activity by lowering the energy barrier for electron transfer to oxygen intermediates. This effect is critical for activating molecular oxygen in both the ORR and OER.[36,37] The valence states of the catalyst elements were probed by X-ray Photoelectron Spectroscopy (XPS) analysis. The XPS spectrum of CeO_2–Fe_xO/NC (Fig. S6a†) confirmed the presence of Fe, Ce, N, O, and C elements. In the high-resolution C 1s spectrum (Fig. 3c), the C–N peak at 285.5 eV indicates successful nitrogen incorporation into the carbon matrix. The nitrogen content of different samples obtained through XPS analysis (Table S3†) shows that CeO_2–Fe_xO/NC has the highest nitrogen content among the three catalysts. This difference indicates that PM can provide nitrogen atoms to the material during the pyrolysis process, highlighting the role of PM in nitrogen doping during material synthesis. The N 1s spectrum (Fig. S6b†) was deconvoluted into five peaks, corresponding to different nitrogen species: pyridinic nitrogen (397.26 eV), metal–nitrogen (Fe–N_x, 398.25 eV), pyrrolic nitrogen (399.94 eV), graphitic nitrogen (400.93 eV), and oxidized nitrogen (403.90 eV).[38] Compared to Ce–Fe_xO/NC samples, the N 1s peak of CeO_2–Fe_xO/NC shifted approximately 0.11 eV to a higher binding energy, suggesting that PM and CeO_2 modify the electronic configuration of the M–N bonds in CeO_2–Fe_xO/NC. This leads to charge transfer from the nitrogen-doped carbon matrix to the metal phase through strong M–N_x interactions.[24] The electrical conductivity of the CeO_2–Fe_xO/NC catalyst was also evaluated (Fig. S6c†). The conductivity value was found to be 0.236 S mm^{-1}, which is higher than that of Ce–Fe_xO/NC (0.132 S mm^{-1}), Fe_xO/NC (0.039 S mm^{-1}), and NC (0.0008 S mm^{-1}) samples. This significant improvement in conductivity is attributed to the presence of multivalent Fe, which enhances the material's ability to facilitate rapid electron transfer on its surface.[39]

In the Fe 2p XPS spectrum (Fig. 3e), two characteristic peaks were observed, corresponding to Fe^{2+} (709.28 eV and 723.40 eV) and Fe^{3+} (711.82 eV and 726.73 eV) states.[40] However, no zero-valent Fe (Fe^0) was detected, as XPS detects only the surface valence states. The Ce 3d spectrum (Fig. 3f) shows characteristic peaks for Ce^{3+} (885.99 eV, 897.25 eV, and 904.25 eV) and Ce^{4+} (882.65 eV, 890.37 eV, 900.75 eV, 908.32 eV, and 916.28 eV).[41] Notably, the Fe^{3+} peak in the CeO_2–Fe_xO/NC sample shifted by about 0.30 eV towards a lower binding energy compared to that of Ce–Fe_xO/NC and Fe_xO/NC samples. This indicates that Ce and PM play a role in electron redistribution, causing Fe to gain more electrons, form reduced Fe, and expand the Fe valence states (from Fe^{3+} to Fe^0).[42,43] Furthermore, compared to Ce–Fe_xO/NC, the Ce^{3+} and Ce^{4+} peaks in the CeO_2–Fe_xO/NC sample shifted by approximately 0.40 eV to higher binding energies, indicating that nitrogen incorporation promotes electron transfer from Ce to Fe, thereby contributing to the formation of multivalent Fe. The surface charge transfer diagram

for CeO_2–Fe_xO/NC, depicted in Fig. 3d, demonstrates these electron transfer phenomena, which are consistent with reports from the literature on similar systems.[17,44]

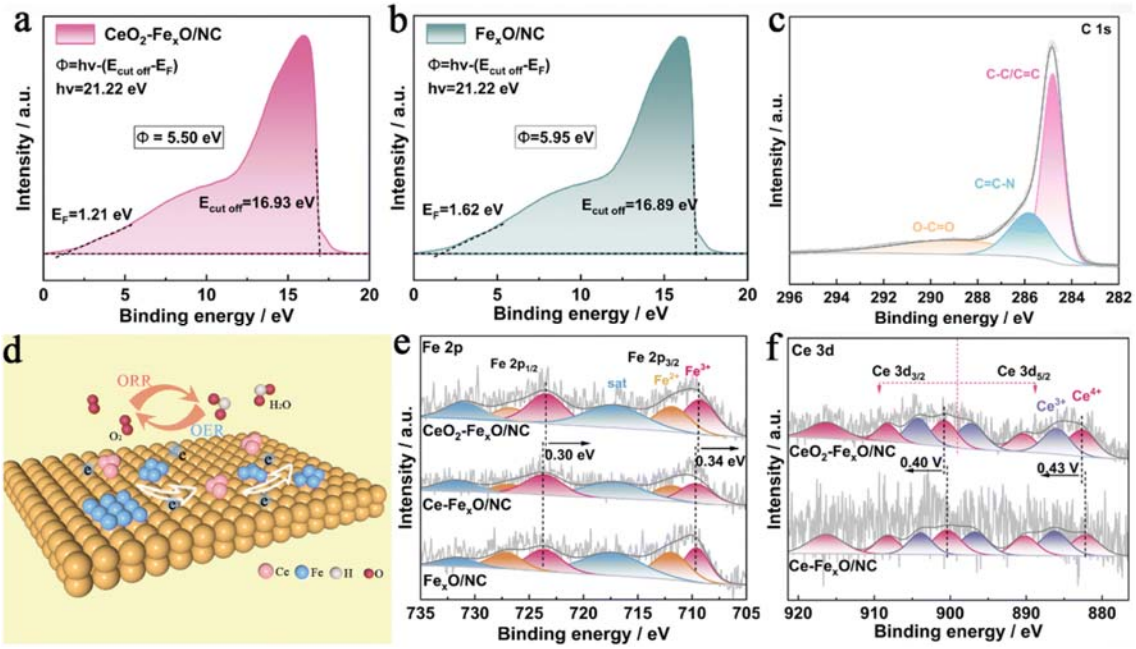

Fig. 3 UPS spectra of (a) CeO_2–Fe_xO/NC and (b) Fe_xO/NC samples. (c) C 1s spectra, (d) schematic of electron transfer, (e) Fe 2p spectra, and (f) Ce 3d spectra.

The ORR catalytic activity of the CeO_2–Fe_xO/NC catalyst was assessed in a 0.1 M KOH electrolyte using a three-electrode setup. As shown in Fig. S7a,† under O_2-saturated conditions, the CeO_2–Fe_xO/NC sample exhibited the most positive oxygen reduction peak, indicating superior ORR catalytic activity. The linear sweep voltammetry (LSV) curves (Fig. 4a) and the corresponding analysis (Fig. 4b) reveal that the CeO_2–Fe_xO/NC catalyst has a half-wave potential ($E_{1/2}$) of 0.89 V and a kinetic current density (J_k) of 19.7 mA cm^{-2} at 0.80 V, which are higher than those of Pt/C ($E_{1/2}$ = 0.86 V, J_k = 6.3 mA cm^{-2}) and other catalysts, demonstrating its enhanced ORR performance. The Tafel slope of CeO_2–Fe_xO/NC (58.2 mV dec^{-1}) is lower than that of Pt/C (64.2 mV dec^{-1}) and other catalysts (Fig. S7b†), suggesting that the formation of multivalent Fe enhances the ORR kinetics of CeO_2–Fe_xO/NC.[45] Further ORR performance was evaluated using a rotating ring-disk electrode (RRDE) setup. The results in Fig. 4c show that the CeO_2–Fe_xO/NC catalyst exhibits a low H_2O_2 yield of only 2.36% within the voltage range of 0.2–1.0 V, with an electron transfer number close to 4, indicating an efficient four-electron transfer process. The stability of the CeO_2–Fe_xO/NC sample was also assessed using the accelerated durability test (ADT) curve (Fig. S7c†), where the half-wave potential shifted by only 18 mV after multiple cycles, indicating good ORR stability. In comparison, the Ce–Fe_xO/NC sample exhibited a 20 mV shift under the same conditions (Fig. S11a†), highlighting the superior ORR stability of CeO_2–Fe_xO/NC.

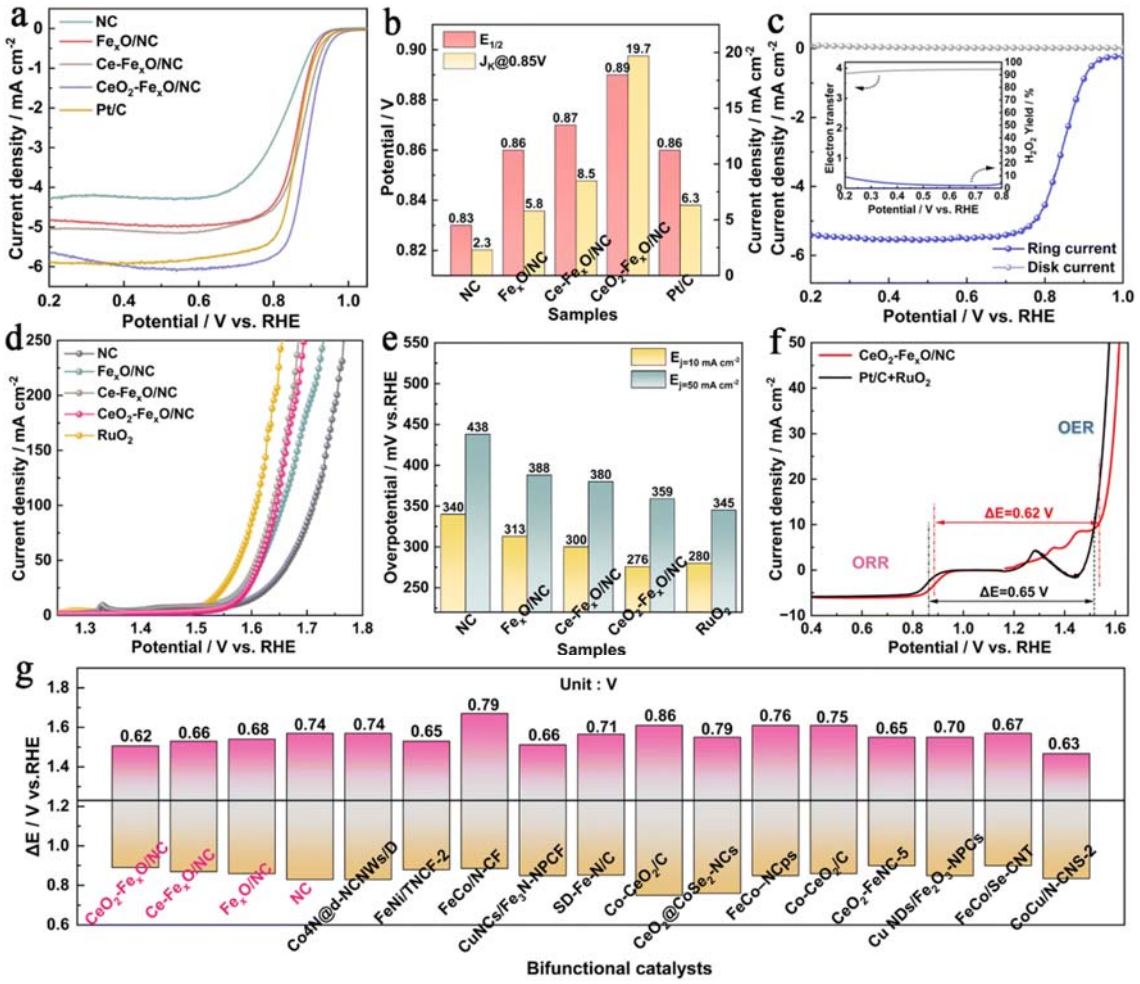

Fig. 4 (a) LSV curves for the ORR. (b) Comparison of the half-wave potential ($E_{1/2}$) and the kinetic current density (J_k) for the ORR. (c) H_2O_2 yield and the electron transfer numbers for the ORR. (d) LSV curves for the OER. (e) Comparison of overpotentials for the OER. (f) Comparison of bifunctional catalytic activity for the ORR and OER. (g) Comparison of CeO_2–Fe_xO/NC from this work with previously reported catalysts from the literature.

The OER activity of the CeO_2–Fe_xO/NC catalyst was analyzed in a 1 M KOH electrolyte. The LSV curves of all prepared catalysts, including commercial RuO_2, are shown in Fig. 4d. As shown in Fig. 4e, the overpotential of the CeO_2–Fe_xO/NC catalyst at 10 mA cm^{-2} is 276 mV (359 mV at 50 mA cm^{-2}), which is comparable to the OER performance of commercial RuO_2 (280 mV and 345 mV) and lower than that of other catalysts. The Tafel slope of the CeO_2–Fe_xO/NC catalyst (99.18 mV dec^{-1}) is lower than that of RuO_2 (100.71 mV dec^{-1}), indicating faster OER kinetics for CeO_2–Fe_xO/NC (Fig. S8a†). Electrochemical impedance spectroscopy (EIS) results (Fig. S8b†) show that the CeO_2–Fe_xO/NC catalyst has the lowest charge transfer resistance (R_{ct}) value of 14.11 Ω, indicating superior charge transfer kinetics due to the interfacial electric field.[46] Additional performance tests were conducted for the samples with different metal molar ratios (Fig. S9 and S10†). The CeO_2–Fe_xO/NC catalyst with an Fe : Ce molar ratio of 10 : 1 displayed the best catalytic activity. After undergoing 5500 cyclic voltammetry (CV) cycles, the LSV curve of CeO_2–Fe_xO/NC showed only a 17 mV shift at 50 mA cm^{-2} (Fig. S8c†), confirming its excellent stability during the OER process. The bifunctional catalytic performance of the CeO_2–Fe_xO/NC sample was evaluated from the

potential difference (ΔE) ($\Delta E = E_{j=10mA\ cm^{-2}} - E_{1/2}$) between the ORR and OER.[47] The ΔE of CeO_2–Fe_xO/NC was found to be 0.62 V (Fig. 4f), which is lower than that of commercial Pt/C + RuO_2 catalysts (ΔE = 0.65 V). In this study, compared to other catalysts, CeO_2–Fe_xO/NC benefits from the combined effects of PM and CeO_2 in regulating the oxidation state of Fe, significantly optimizing the electronic structure and the distribution of active sites within the catalyst. Consequently, CeO_2–Fe_xO/NC achieves outstanding catalytic activity. When compared to bifunctional catalysts that were recently reported (Fig. 4g and Table S4†), the CeO_2–Fe_xO/NC sample still exhibits excellent oxygen electrocatalytic performance.

In situ Raman spectroscopy (Fig. 5a) was conducted to reveal the dynamic changes of oxygen intermediates at the active sites of CeO_2–Fe_xO/NC at varying potentials. Based on literature references, the signal peak at 728 cm^{-1} belongs to the O–O stretching vibration of the OOH* species adsorbed on the active site,[48,49] while the peak at 1056 cm^{-1} is attributed to the O–O stretching vibration of $*O_2^-$ adsorbed on the Fe active site.[50,51] Both OOH* and $*O_2^-$ are important intermediates in the ORR process. Throughout the entire voltage range, the Raman peaks corresponding to the D and G bands, which are associated with the carbon structure, remained unchanged (Fig. 5d). This stability suggests that the new peaks observed in the spectra are due to the oxygen-containing groups involved in the electrocatalytic process, rather than changes in the carbon matrix itself.[52] Notably, magnified Raman spectra in Fig. 5b and c reveal that the peak at 728 cm^{-1} corresponding to OOH* appears at a potential of 2.4 V, while the peak at 1060 cm^{-1}, which corresponds to $*O_2^-$, first appears at 2.0 V and remains stable as the potential decreases further. This behavior indicates that the oxygen intermediates at the active sites of the CeO_2–Fe_xO/NC catalyst exhibit higher ORR reactivity and good stability at lower potentials.[53] Therefore, under alkaline conditions, the key intermediates in the ORR catalyzed by CeO_2–Fe_xO/NC are *OOH and $*O_2^-$, with $*O_2^-$ protonating to form *OOH. This process is identified as the rate-determining step (RDS) in the ORR, thus confirming that the $4e^-$ transfer mechanism dominates in the catalytic process.

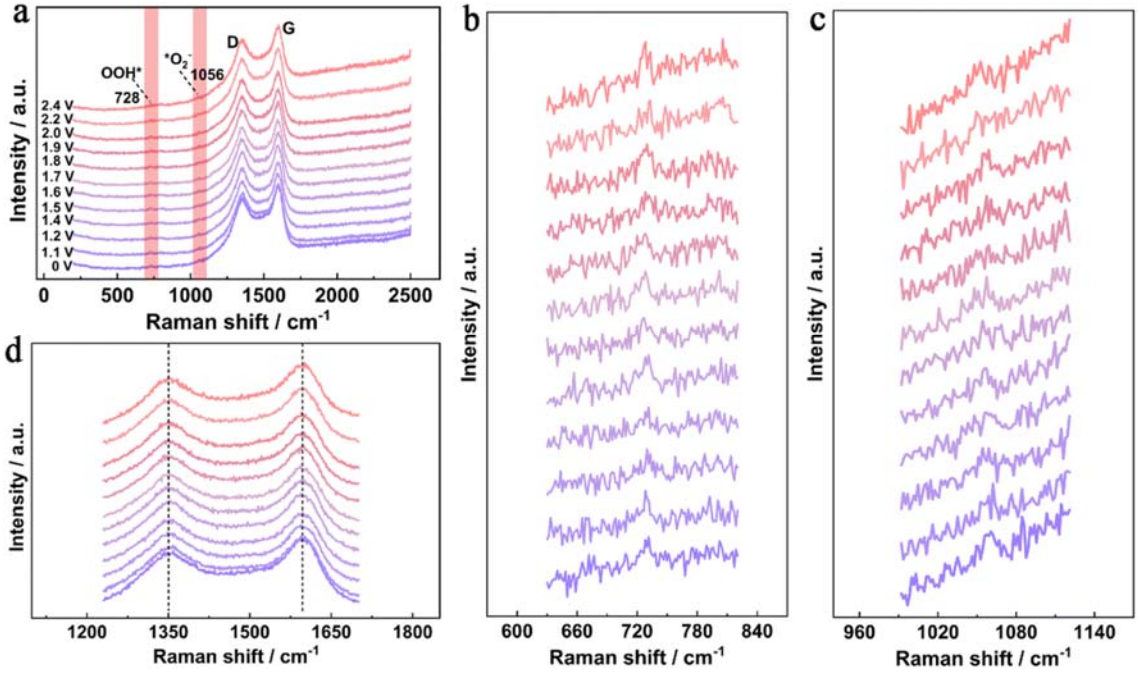

Fig. 5 (a) *In situ* Raman spectra of the CeO_2–Fe_xO/NC surface ORR at different potentials. (b–d) The local magnified images near the peaks at 728 cm^{-1} and 1056 cm^{-1}, as well as around the D and G peaks.

The electrochemical performance of the CeO_2–Fe_xO/NC catalyst was further investigated by assembling a rechargeable zinc–air battery (ZAB) and comparing it to a Pt/C + RuO_2-based ZAB. The open-circuit voltage (OCV) of the CeO_2–Fe_xO/NC-based ZAB, as shown in Fig. 6b, is 1.46 V, which is higher than that of the Pt/C + RuO_2-based ZAB (1.42 V). When the current density was varied between 1 and 60 mA cm^{-2} and then returned to 1 mA cm^{-2}, the discharge voltage of the CeO_2–Fe_xO/NC-based ZAB recovered rapidly with minimal decline (Fig. 6c), indicating the excellent rate performance and reversibility of the CeO_2–Fe_xO/NC catalyst.[54] The discharge polarization and power density curves at various current densities (Fig. 6d) reveal that the peak power densities of CeO_2–Fe_xO/NC and Pt/C + RuO_2 were 108.2 mW cm^{-2} and 85.2 mW cm^{-2}, respectively, demonstrating superior activity and rechargeability of the CeO_2–Fe_xO/NC-based ZAB. Additionally, the constant current discharge curve at 10 mA cm^{-2} (Fig. 6e) shows that the CeO_2–Fe_xO/NC-based ZAB discharged for a longer time at a higher voltage platform. The specific capacity of the CeO_2–Fe_xO/NC-based battery was 743.0 mA h g^{-1}, which is closer to the theoretical maximum value of 820 mA h g^{-1}, outperforming the Pt/C + RuO_2-based ZAB, which had a specific capacity of 474.2 mA h g^{-1}. Long-term discharge stability tests (Fig. 6f) were conducted to assess the performance of the CeO_2–Fe_xO/NC-based ZAB at 10 mA cm^{-2}.[55] The discharge stability of the CeO_2–Fe_xO/NC-based ZAB was maintained for 200 h, and after three zinc foil replacements, the battery voltage retention rate was 97.5%, which is higher than the voltage retention rate (94.2%) of the Ce–Fe_xO/NC-based ZAB under the same discharge conditions (Fig. S11b†). This demonstrates the excellent discharge stability of the CeO_2–Fe_xO/NC-based ZAB. In addition, the performance of other ZAB catalysts is listed in Table S5.† Overall, the CeO_2–Fe_xO/NC-based ZAB demonstrates outstanding battery performance, highlighting the significant potential of the CeO_2–Fe_xO/NC electrocatalyst for practical ZAB applications.

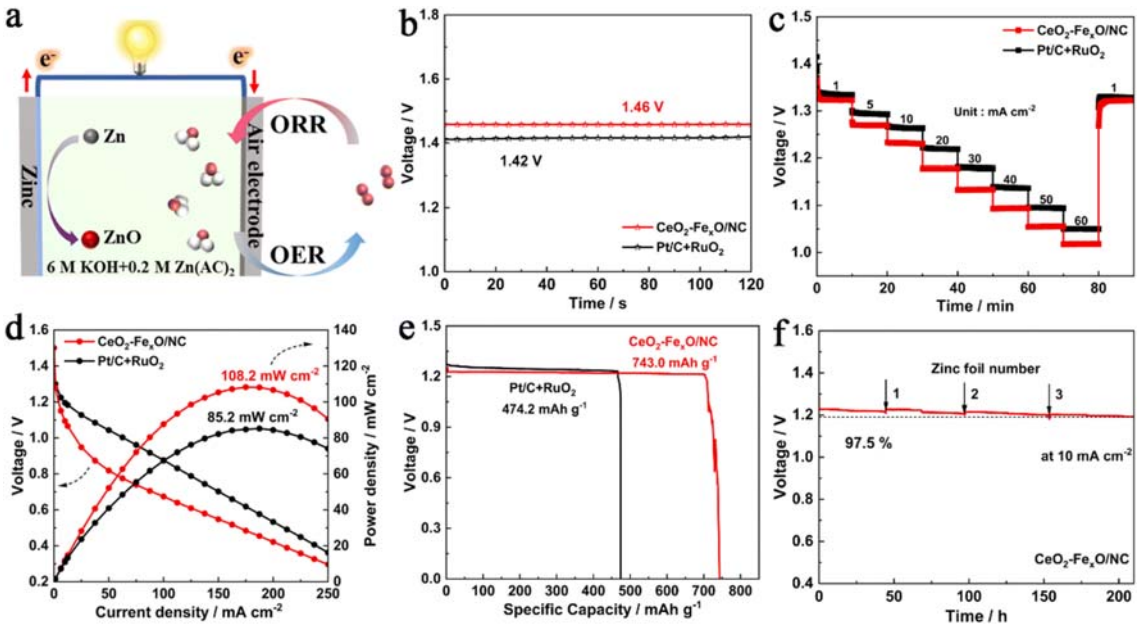

Fig. 6 (a) Schematic diagram of the rechargeable ZAB structure, (b) open-circuit voltage curves, (c) constant current discharge curves at different current densities, (d) discharge polarization curves and corresponding power density curves, (e) voltage and specific capacity curves at 10 mA cm^{-2}, and (f) the long-term discharge curve at 10 mA cm^{-2}.

The experimental results confirm that the synthesized CeO_2–Fe_xO/NC catalyst exhibits remarkable performance for both the ORR and OER. Key intermediates in the ORR process were identified *via in situ* Raman spectroscopy, showing that oxygen-containing species (*O_2^- and *OOH) are adsorbed on the Fe active sites, facilitating the reversible ORR/OER processes. The surface structure of CeO_2–Fe_xO/NC plays a crucial role in its performance. The three-dimensional porous nanostructure provides an efficient pathway for electron transfer and enhances mass transport. Its high surface area offers favorable conditions for the effective dispersion of active sites. Additionally, the electron modulation in CeO_2–Fe_xO/NC significantly contributes to catalytic activity. The incorporation of CeO_2 and nitrogen (N) results in electron donation to Fe, increasing the charge density of Fe, thereby modulating the electronic distribution at the interface. The introduction of PM and CeO_2 leads to the formation of multivalent Fe and further enhances the catalyst's performance. Furthermore, compared to Fe_xO/NC, CeO_2–Fe_xO/NC exhibits a lower work function, suggesting that it provides a lower electronic energy barrier for electron transfer from the surface to the oxygen intermediates. This results in enhanced intrinsic activity for both the ORR and OER, further demonstrating its potential for use in energy storage and conversion applications.

Conclusions

This study presents the development of a bimetallic catalyst (CeO_2–Fe_xO/NC), which consists of CeO_2-regulated multivalent Fe_xO nanoparticles. The catalyst is supported on a carbon substrate and incorporates Fe species in different oxidation states (Fe^0, Fe^{2+}, and Fe^{3+}). *In situ* Raman spectroscopy was employed to identify the active sites responsible for the oxygen reduction reaction (ORR). The analysis revealed that under alkaline conditions, the key intermediates *O^{2-} and *OOH are adsorbed on the active sites, confirming the structural stability of the catalyst during the catalytic process. Furthermore, the formation of multivalent Fe and the modulation of the electronic structure significantly enhance both the ORR and oxygen evolution reaction (OER) performances. Specifically, the introduction of N and Ce atoms results in electron donation to the Fe sites, preventing the over-oxidation of Fe. The multivalent Fe enhances electron transfer, which reduces the adsorption of oxygen intermediates. Additionally, the catalyst's lower work function suggests that CeO_2–Fe_xO/NC can offer a reduced energy barrier for electron transfer, thereby improving catalytic activity. As a cathode catalyst for zinc–air batteries (ZABs), CeO_2–Fe_xO/NC-based ZABs exhibit exceptional discharge stability, with performance sustained for over 200 h. Overall, the synthesis of non-precious metal carbon-based catalysts modified with multivalent metal elements demonstrates significant practical applicability towards real-world applications.

Data availability

The authors declare that all data supporting the findings of this study are available within the paper and its ESI.†

Author contributions

Jiao Peng was involved in conceptualization, methodology development, investigation, formal analysis, data curation, visualization, as well as writing and editing. Zining Wang contributed to visualization efforts. Jianwei Ren performed formal analysis, assisted with visualization, and participated in writing, review, and editing. Yudong He contributed to the investigation, while Jiahao Li focused on validation. Shichang Xin provided support in visualization tasks, and

Xuyun Wang contributed to methodology development and visualization. Hui Wang undertook responsibilities in conceptualization, supervision, writing, review, editing, and securing funding. Rongfang Wang contributed through conceptualization, methodology development, and supervision.

Conflicts of interest

There are no conflicts to declare.

Acknowledgements

The authors extend their gratitude to the Open Project Program of the Guangdong Provincial Key Laboratory for Electronic Functional Materials and Devices at Huizhou University (Grant No. EFMD2021001Z) and the Natural Science Foundation of Shandong Province, China (Grant No. ZR2022MB118), for their financial support of this work.

References

1. G.-L. Li , G.-C. Cheng , B.-B. Yang , C.-D. Liu , L.-F. Yuan , W.-W. Chen , X.-C. Xu and C. Hao , *Int. J. Hydrogen Energy*, 2018, **43** , 19451 —19459.
2. W. Zhou , B. Li , X. Liu , J. Jiang , S. Bo , C. Yang , Q. An , Y. Zhang , M. A. Soldatov , H. Wang , S. Wei and Q. Liu , *Nat. Commun.*, 2024, **15** , 6650.
3. Y. Wang , N. Katyal , Y. Tang , H. Li , K. Shin , W. Liu , R. He , M. Xu , G. Henkelman and S.-J. Bao , *Small*, 2024, **20** , 2306504.
4. S. Wang , Z. Li , W. Duan , P. Sun , J. Wang , Q. Liu , L. Zhang and Y. Zhuang , *J. Energy Chem.*, 2023, **86** , 41 —53.
5. J. Feng , D. Zheng , R. Yin , X. Niu , X. Xu , S. Meng , S. Ma , W. Shi , F. Wu , W. Liu and X. Cao , *Small Struct.*, 2023, **4** , 2200340.
6. H. Li , W. Wang , S. Xue , J. He , C. Liu , G. Gao , S. Di , S. Wang , J. Wang , Z. Yu and L. Li , *J. Am. Chem. Soc.*, 2024, **146** , 9124 —9133.
7. X.-T. Wang , T. Ouyang , L. Wang , J.-H. Zhong , T. Ma and Z.-Q. Liu , *Angew Chem. Int. Ed. Engl.*, 2019, **58** , 13291 —13296.
8. Z. Li , S. Ji , C. Wang , H. Liu , L. Leng , L. Du , J. Gao , M. Qiao , J. H. Horton and Y. Wang , *Adv. Mater.*, 2023, **35** , 2300905.
9. J. Kuang , Y. Shen , Y. Zhang , J. Yao , J. Du , S. Yang , S. Zhang , Y. Fang and X. Cai , *Small*, 2023, **19** , 2207413.
10. D. Ye , Y. Shen , H. Mao , Y. Liang , Q. Gao , S. Yang , S. Zhang , X. Cai and Y. Fang , *Chem. Eng. J.*, 2023, **464** , 142601.
11. W. Cheng , P. Yuan , Z. Lv , Y. Guo , Y. Qiao , X. Xue , X. Liu , W. Bai , K. Wang , Q. Xu and J. Zhang , *Appl. Catal., B*, 2020, **260** , 118198.
12. Y. Zhan , F. Xie , H. Zhang , Y. Jin , H. Meng , J. Chen and X. Sun , *ACS Appl. Mater. Interfaces*, 2020, **12** , 17481 —17491.
13. H. Li , S. Di , P. Niu , S. Wang , J. Wang and L. Li , *Energy Environ. Sci.*, 2022, **15** , 1601 —1610.
14. H.-S. Fan , F.-X. Ma , Z.-H. Liu , W.-H. Wang , Z.-Q. Liu , X.-Y. Liang , Y. Du , Y.-Y. Li , L. Zhen and C.-Y. Xu , *Rare Met.*, 2024, **43** , 5769 —5780.
15. T. Chen , J.-H. Dou , L. Yang , C. Sun , N. J. Libretto , G. Skorupskii , J. T. Miller and M. Dincă , *J. Am. Chem. Soc.*, 2020, **142** , 12367 —12373.
16. Y. Shen , H. Mao , C. Li , K. Li , Y. Liu , J. Liao , S. Zhang , Y. Fang and X. Cai , *Adv. Fiber Mater.*, 2024, **6** , 1470 —1482.
17. M. Zhang , R. Sun , G. Long , C. Zhou , Y. Zhou , M. Chen , X. Huang , G. Han , X. Xu , H. Shi and W. Zhao , *Int. J. Hydrogen Energy*, 2018, **43** , 8313 —8322.

18. R. Zhao , X. Chi , X. Wang , L. Zhao , Y. Zhou , Y. Xiong , S. Yao , S. Wang , D. Wang , Z. Fu , Z. Yang and Y.-M. Yan , *J. Mater. Chem. A*, 2022, **10** , 10219 —10226.
19. T. Ye , K. Ba , X. Yang , T. Xiao , Y. Sun , H. Liu , C. Tang , B. Ge , P. Zhang , T. Duan and Z. Sun , *Chem. Eng. J.*, 2023, **452** , 139515.
20. Y. Nosaka , S. Takahashi , H. Sakamoto and A. Y. Nosaka , *J. Phys. Chem. C*, 2011, **115** , 21283 —21290.
21. A. Petala , E. Ioannidou , A. Georgaka , K. Bourikas and D. I. Kondarides , *Appl. Catal., B*, 2015, **178** , 201 —209.
22. G. D. Moon , J. B. Joo , I. Lee and Y. Yin , Decoration of size-tunable CuO nanodots on TiO_2 nanocrystals for noble metal-free photocatalytic H_2 production, *Nanoscale*, 2014, **6** , 12002 —12008.
23. Z. Guan , J. Li , S. Li , K. Wang , L. Lei , Y. Wang , L. Zhuang and Z. Xu , *Small Methods*, 2024, **8** , 2301419.
24. X. Li , L. Li , G. Chen , X. Chu , X. Liu , C. Naisa , D. Pohl , M. Löffler and X. Feng , *Nat. Commun.*, 2023, **14** , 4034.
25. Q. Wu , J. Liang , M. Xiao , C. Long , L. Li , Z. Zeng , A. Mavrič , X. Zheng , J. Zhu , H.-W. Liang , H. Liu , M. Valant , W. Wang , Z. Lv , J. Li and C. Cui , *Nat. Commun.*, 2023, **14** , 997.
26. Q. Dong , Z. Mo , H. Wang , S. Ji , X. Wang , V. Linkov and R. Wang , *ACS Sustain. Chem. Eng.*, 2020, **8** , 6979 —6989.
27. P. He , M.-Y. Hu , J.-H. Li , T.-Z. Qiao , Y.-L. Lu and S.-F. Zhu , *Natl. Sci. Rev.*, 2023, 10.1093/nsr/nwad324 **11**.
28. L. Wan , Z. Xu , Q. Cao , Y. Liao , B. Wang and K. Liu , *Nano Lett.*, 2022, **22** , 4535 —4543.
29. Y. Yang , B. Li , Y. Liang , W. Ni , X. Li , G. Shen , L. Xu , Z. Chen , C. Zhu , J.-X. Liang and S. Zhang , *Adv. Sci.*, 2024, **11** , 2310231.
30. F.-D. Tu , Z.-Y. Wu , P. Guo , L.-X. Shen , Z.-Y. Zhang , Y.-K. Dai , M. Ma , J. Liu , B. Xu , Y.-L. Zhang , L. Zhao and Z.-B. Wang , *J. Colloid Interface Sci.*, 2023, **637** , 10 —19.
31. J. Liu , J. Yin , Y. Lin , M. Pang , H. Pang , S. Zhang , L. Xu , J. Yang and Y. Tang , *Nano Res.*, 2025, **18** , 94907016.
32. J. Sheng , S. Sun , G. Jia , S. Zhu and Y. Li , *ACS Nano*, 2022, **16** , 15994 —16002.
33. S. Li , T. Liu , W. Zhang , M. Wang , H. Zhang , C. Qin , L. Zhang , Y. Chen , S. Jiang , D. Liu , X. Liu , H. Wang , Q. Luo , T. Ding and T. Yao , *Nat. Commun.*, 2024, **15** , 3416.
34. H. Xu , J. Yang , R. Ge , J. Zhang , Y. Li , M. Zhu , L. Dai , S. Li and W. Li , *J. Energy Chem.*, 2022, **71** , 234 —265.
35. H. Wang , X. Liu , P. Niu , S. Wang , J. Shi and L. Li , *Matter*, 2020, **2** , 1377 —1413.
36. Y. Fan , R. Li , C. Zhao , A. Hu , B. Zhou , Y. Pan , J. Chen , Z. Yan , M. Liu , M. He , J. Liu , N. Chen and J. Long , *J. Colloid Interface Sci.*, 2023, **645** , 439 —447.
37. Z. Wu , Y. Zhang , L. Li , Y. Zhao , Y. Shen , S. Wang and G. Shao , *J. Mater. Chem. A*, 2020, **8** , 23248 —23256.
38. Q. Dong , H. Wang , J. Ren , X. Wang and R. Wang , *Chem. Eng. J.*, 2022, **442** , 136128.
39. Q. Wang , J. Su , H. Chen , D. Wang , X. Tian , Y. Zhang , X. Feng , S. Wang , J. Li and H. Jin , *Adv. Funct. Mater.*, 2022, **32** , 2209201.
40. T. Yamashita and P. Hayes , *Appl. Surf. Sci.*, 2008, **254** , 2441 —2449.
41. Z. Liu , J. Wan , M. Li , Z. Shi , J. Liu and Y. Tang , *Nanoscale*, 2022, **14** , 1997 —2003.
42. X. Zou , Q. Lu , J. Wu , K. Zhang , M. Tang , B. Wu , S. She , X. Zhang , Z. Shao and L. An , *Adv. Funct. Mater.*, 2024, **34** , 2401134.
43. E. Bianchetti , D. Perilli and C. Di Valentin , *ACS Catal.*, 2023, **13** , 4811 —4823.
44. Y. Huang , Y. Liu , Y. Deng , J. Zhang , B. He , J. Sun , Z. Yang , W. Zhou and L. Zhao , *J. Colloid Interface Sci.*, 2022, **625** , 839 —849.
45. Q. Dong , G. Li , F. Liu , J. Ren , H. Wang and R. Wang , *Appl. Catal., B*, 2023, **326** , 122415.
46. Y. Li , P. Zhang , L. Wan , Y. Zheng , X. Qu , H. Zhang , Y. Wang , K. Zaghib , J. Yuan , S. Sun , Y. Wang , Z. Zhou and S. Sun , *Adv. Funct. Mater.*, 2021, **31** , 2009645.
47. J. Barrio , A. Pedersen , S. C. Sarma , A. Bagger , M. Gong , S. Favero , C.-X. Zhao , R. Garcia-Serres , A. Y. Li , Q. Zhang , F. Jaouen , F. Maillard , A. Kucernak , I. E. L. Stephens and M.-M. Titirici , *Adv. Mater.*, 2023, **35** , 2211022.

48. Y.-L. A , Z.-Y. Du , H.-J. Ze , X.-T. Wang , Y. Zhang , H. Zhang , Q.-N. Zheng , J.-C. Dong , J.-H. Tian and J.-F. Li , *Electrochem.*, 2023, **42** , 101381.
49. Y.-L. Sun , Y.-L. A , M.-F. Yue , H.-Q. Chen , H. Ze , Y.-H. Wang , J.-C. Dong , Z.-Q. Tian , P.-P. Fang and J.-F. Li , *Anal. Chem.*, 2022, **94** , 4779 —4786.
50. J.-C. Dong , M. Su , V. Briega-Martos , L. Li , J.-B. Le , P. Radjenovic , X.-S. Zhou , J. M. Feliu , Z.-Q. Tian and J.-F. Li , *J. Am. Chem. Soc.*, 2020, **142** , 715 —719.
51. J. Wei , D. Xia , Y. Wei , X. Zhu , J. Li and L. Gan , *ACS Catal.*, 2022, **12** , 7811 —7820.
52. Q. Wu , H. Zou , X. Mao , J. He , Y. Shi , S. Chen , X. Yan , L. Wu , C. Lang , B. Zhang , L. Song , X. Wang , A. Du , Q. Li , Y. Jia , J. Chen and X. Yao , *Nat. Commun.*, 2023, **14** , 6275.
53. L. Lyu , X. Hu , S. Lee , W. Fan , G. Kim , J. Zhang , Z. Zhou and Y.-M. Kang , *J. Am. Chem. Soc.*, 2024, **146** , 4803 —4813.
54. Y. He , W. Shang , M. Ni , Y. Huang , H. Zhao and P. Tan , *Chem. Eng. J.*, 2022, **427** , 130862.
55. L. Song , T. Zheng , L. Zheng , B. Lu , H. Chen , Q. He , W. Zheng , Y. Hou , J. Lian , Y. Wu , J. Chen , Z. Ye and J. Lu , *Appl. Catal., B*, 2022, **300** , 120712.